Water-Soluble MnO Nanocolloid for a Molecular T_1 MR Imaging: A Facile One-Pot Synthesis, In vivo T_1 MR Images, and Account for Relaxivities

Myung Ju Baek,[†] Ja Young Park,[‡] Wenlong Xu,[‡] Krishna Kattel,[‡] Han Gyeol Kim,[‡] Eun Jung Lee,[‡] Anilkumar Kantilal Patel,[‡] Jae Jun Lee,[||] Yongmin Chang,*[,†,||] Tae Jeong Kim,[†,⊥] Ji Eun Bae,[§] Kwon Seok Chae,[§] and Gang Ho Lee*[,†,‡]

Department of Nanoscience and Nanotechnology, Department of Chemistry, College of Natural Sciences, Department of Applied Chemistry, College of Engineering, and Department of Biology Education, Teachers' College, Kyungpook National University, Taegu 702-701, South Korea, and Department of Molecular Medicine and Medical & Biological Engineering, School of Medicine, Kyungpook National University and Hospital, Taegu 702-701, South Korea

ABSTRACT A facile one-pot synthesis of a water-soluble MnO nanocolloid (i.e., D-glucuronic acid-coated MnO nanoparticle) is presented. The MnO nanoparticle in the MnO nanocolloid was coated with a biocompatible and hydrophilic D-glucuronic acid, and its particle diameter was nearly monodisperse and ranged from 2 to 3 nm. The average hydrodynamic diameter of the MnO nanocolloid was estimated to be 5 nm. The MnO nanoparticle was nearly paramagnetic down to $T = 3$ K. The MnO nanocolloid showed a high longitudinal water proton relaxivity of $r_1 = 7.02\ s^{-1}\ mM^{-1}$ with the r_2/r_1 ratio of 6.83 due to five unpaired S-state electrons of Mn(II) ion ($S = 5/2$) as well as a high surface to volume ratio of the MnO nanoparticle. High contrast in vivo T_1 MR images were obtained for various organs, showing the capability of the MnO nanocolloid as a sensitive T_1 MRI contrast agent. The suggested three key-parameters which control the r_1 and r_2 relaxivities of nanocolloids (i.e., the S value of a metal ion, the spin structure, and the surface to volume ratio of a nanoparticle) successfully accounted for the observed r_1 and r_2 relaxivities of the MnO nanocolloid.

KEYWORDS: MnO nanocolloid • one-pot synthesis • water proton relaxivity • MRI contrast agent • in vivo T_1 MR image

1. INTRODUCTION

Magnetic nanocolloids have been applied to a variety of biological and biomedical areas so far. These include the immobilization (1, 2) or bioseparation (2−4) of biological molecules such as proteins, peptides, and enzymes, the drug or the gene delivery (2, 4, 5), the magnetic resonance imaging (MRI) (2, 4, 5), the hyperthermia (2, 4, 5), and so on. Among these applications, application to MRI contrast agents has been a hot issue. The MRI is a noninvasive technique that is used to diagnose diseases. The MRI can be further improved by using a MRI contrast agent (6, 7).

Magnetic nanocolloids can possess higher water proton relaxivities than molecular chelates because metal ions in a nanoparticle are densely populated. Thus, they can be used as sensitive MRI contrast agents. Various magnetic nanocolloids as MRI contrast agents have been studied so far. These include the iron oxide (2, 5, 8), the ferrite (9), the manganese oxide (10), the gadolinium oxide (11−19), the gadolinium compound (20−24), and the dysprosium oxide nanocolloids (24, 25). Among these, only the iron oxide nanocolloid is now clinically applied as a T_2 MRI contrast agent (8). The others are also promising candidates for clinical use as either T_1 or T_2 MRI contrast agents because of their high longitudinal (r_1) or transverse (r_2) water proton relaxivities, respectively.

This work deals with a water-soluble MnO nanocolloid with a monodisperse core particle diameter (d) ranging from 2 to 3 nm. The magnetic nanocolloids with the d in this size range will be very useful as T_1 MRI contrast agents because first of all, they can be easily excreted through kidneys because of their small sizes (14), which is an essential requirement for clinical application, and because they can have high r_1 relaxivities due to their high surface to volume ratio (P), as observed in the Gd_2O_3 nanocolloid (16). This is because only the surface (not inside) metal ions in a nanoparticle are mainly active for the longitudinal water proton relaxation (16). In the case of the Gd_2O_3 nanocolloid, the optimal d for the maximal r_1 relaxivity was found to be between 1.0 and 2.5 nm (16). This is opposite to a T_2 MRI contrast agent, which has a somewhat large d. This is

* Corresponding author. Tel: -82-53-950-5340 (G.H.L.);. Fax: -82-53-950-6330. E-mail: ghlee@mail.knu.ac.kr. (G.H.L.); ychang@knu.ac.kr (Y.C.).
Received for review July 21, 2010 and accepted September 21, 2010
[†] Department of Nanoscience and Nanotechnology, Kyungpook National University.
[‡] Department of Chemistry, College of Natural Sciences, Kyungpook National University.
[||] Department of Applied Chemistry, College of Engineering, Kyungpook National University.
[⊥] Department of Biology Education, Teachers' College, Kyungpook National University.
[§] Department of Molecular Medicine and Medical & Biological Engineering, School of Medicine, Kyungpook National University and Hospital.
DOI: 10.1021/am100641z

because the magnetic moment (M) which induces the r_2 relaxivity rapidly decreases with decreasing the d (26−28). For this reason, the T_2 MRI contrast agent such as the superparamagnetic iron oxide (SPIO) nanocolloid at least has a d value greater than 5 nm and thus is used only as a liver-specific T_2 MRI contrast agent (8).

In designing a nanocolloidal MRI contrast agent, parameters that control the r_1 and r_2 relaxivities should be well understood. A T_1 MRI contrast agent should have a high r_1 relaxivity and the r_2/r_1 ratio close to one. A T_2 MRI contrast agent, however, should have a high r_2 relaxivity and a large r_2/r_1 ratio. Here, the r_2/r_1 ratio is theoretically always greater than one (29). Three key-parameters were suggested in this work, which include the value of S in which S is the total electron spin of a metal ion, the spin structure, and the P of a nanoparticle in a nanocolloid.

Qualitative descriptions for the three key-parameters are as follows. In case of a T_1 MRI contrast agent, first, each metal ion in a nanoparticle should have a high S value (i.e., a large number of unpaired S-state (not L-state) electrons). This is because a slow electron spin relaxation of S-state electrons closely matches with a water proton spin relaxation, which is also slow. Thus, S-state electrons can efficiently induce the longitudinal water proton relaxation. However, L-state electrons have a fast electron spin relaxation which hardly matches with the water proton spin relaxation. Thus, they can not efficiently induce the longitudinal water proton relaxation (6, 30). Note that the r_1 relaxivity is proportional to the $S(S + 1)$ (7). The Mn(II) ion largely satisfies this because it has $S = 5/2$ and $L = 0$ (31). Second, a nanoparticle should have a paramagnetic spin structure in order to minimize the transverse water proton relaxation. At this condition, the r_2/r_1 ratio is close to one. One example for this is the Gd_2O_3 nanocolloid (11−19). This is because a paramagnetic nanoparticle has $M = 0$. Note that the transverse water proton relaxation is accelerated by a fluctuating local magnetic field produced by the M of a nanoparticle (32, 33). Third, a nanoparticle should have a high P. This is because only the surface metal ions in a nanoparticle are mainly active for the longitudinal water proton relaxation as mentioned before (16). Let us consider a T_2 MRI contrast agent. The T_2 MRI contrast agent should have a large M to have both a high r_2 relaxivity and a high r_2/r_1 ratio, because the r_2 relaxivity is proportional to M^2 (32). To have a large M, first, the S value should be high like a T_1 MRI contrast agent because M is a vector sum of all the $\sqrt{S(S + 1)}$ of metal ions. Second, the spin structure of a nanoparticle should be either ferromagnetic or ferrimagnetic. Third, the P should be small.

In this work, we report a facile one-pot synthesis of a water-soluble MnO nanocolloid with the core d ranging from 2 to 3 nm in a polar organic solvent. The present method is simpler than the synthesis in a nonpolar organic solvent (10, 34) because separation of nanoparticles from the solvent after synthesis is not necessary to coat them with a biocompatible and hydrophilic ligand. We characterized physical properties and performed in vitro and in vivo MRI tests of the MnO nanocolloid to prove their capability as a T_1 MRI contrast agent. We proposed the three key-parameters that control the r_1 and r_2 relaxivities of nanocolloids. By using them, we successfully accounted for the observed r_1 and r_2 relaxivities of the MnO nanocolloid as well as those of the Gd_2O_3 and the SPIO nanocolloids.

2. EXPERIMENTAL PROCEDURES

Chemicals. Manganese chloride tetrahydrate ($MnCl_2.4H_2O$ (99.99%)) as a Mn(II) ion precursor, triethylene glycol (99%) as a solvent, sodium hydroxide (NaOH (99.998%)) as an oxygen source, and D-glucuronic acid (>98%)) as a surface coating ligand were all purchased from Sigma-Aldrich and used without further purification. N_2 (99.99%) as a flowing gas and triply distilled water as a MRI solvent were used.

One-Pot Synthesis of MnO Nanocolloid. Ten millimoles of $MnCl_2.4H_2O$ and 30 mL of triethylene glycol were added to a 100 mL three-necked flask and the mixture was magnetically stirred at room temperature under N_2 gas flow. Separately, 20 mmol of NaOH was dissolved in 10 mL of solvent. The latter solution was slowly added to the former solution through a syringe after the precursor was completely dissolved in the solvent. The reaction temperature was raised to 200 °C and kept at that temperature for 6 h. The reaction temperature was lowered to 140 °C and then, 10 mmol of D-glucuronic acid was added to the reaction solution. The reaction continued for more 24 h. The reaction solution was cooled to room temperature and then, transferred to a 1 L beaker. The solvent, unreacted coating ligand, unreacted Mn(II), and Cl^- ions were removed from the reaction solution by washing it with distilled water three times. To do this, we added 500 mL of distilled water to the reaction solution, and then magnetically stirred it for ∼30 min. The reaction solution was kept for a week or so until the MnO nanocolloid was settled down to the bottom of the solution. The top transparent solution was decanted. This procedure was repeated three times. Half of the MnO nanocolloid was dispersed in distilled water to prepare a MRI solution. The remaining half was dried in air to prepare a powder sample for characterizations.

Characterization. A high-resolution transmission electron microscope (HRTEM) (JEOL, JEM 2100F, 200 kV acceleration voltages) was used to measure the d of the MnO nanoparticle in the MnO nanocolloid. A 200 mesh copper grid covered with an amorphous carbon membrane was placed onto a filter paper and one drop of the MnO nanocolloidal solution diluted in distilled water was placed onto the copper grid by using a micropipet (Eppendorf, 2−20 μL). A dynamic light scattering (DLS) particle size analyzer (UPA-150, Microtrac) was used to measure the hydrodynamic diameter (a) of the MnO nanocolloid. A Fourier transform infrared (FTIR) absorption spectrometer (Mattson Instruments, Inc., Galaxy 7020A) was used to prove the surface coating of the MnO nanoparticle with a D-glucuronic acid. To record a FTIR absorption spectrum (400−4000 cm^{-1}), a pellet was made by pressing a mixture of a powder sample and KBr. A thermogravimetric analysis (TGA) instrument (TA Instruments, SDT Q 600) was used to estimate the amount of surface coating of the MnO nanoparticle in the MnO nanocolloid. The TGA curve of a powder sample was recorded between room temperature and 700 °C while air was flowed. A superconducting quantum interference device (SQUID) magnetometer (Quantum Design, MPMS-7) was used to characterize magnetic properties of the MnO nanoparticle in the MnO nanocolloid. Both $M-H$ curves ($-5 \leq H \leq 5$ T) at temperatures (T) of 5 and 300 K and zero-field-cooled (ZFC) $M-T$ curve ($3 \leq T \leq 330$ K) at an applied field (H) of 100 oersted (Oe) were recorded. To measure these curves, an exact mass (10 − 20 mg) of a powder sample was loaded into a nonmag-

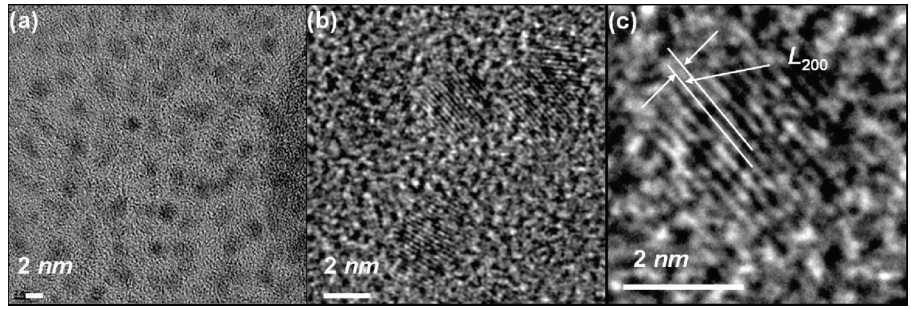

FIGURE 1. (a−c) HRTEM images of the MnO nanocolloid at different magnifications.

netic capsule. A net magnetization of the MnO nanoparticle in the MnO nanocolloid was obtained through the mass correction by using the mass percentage of the MnO nanoparticle in the MnO nanocolloid estimated from the TGA curve.

In vitro Cytotoxicity Test. Both the human prostate cancer (DU145) and the mouse normal hepatocyte (NCTC1469) cell lines were used to measure toxicity of the MnO nanocolloid. Cellular toxicity was quantified by measuring the intracellular ATP by using the CellTiter-Glo Luminescant Cell Viability Assay (Promega, WI, USA) according to the manufacturer's instruction and by using a luminometer (Victor 3, Perkin-Elmer). Cells were seeded on a 24-well cell culture plate at the density of 5×10^4 with a 500 μL volume per well. They were incubated for 24 h (5% CO_2, 37 °C). Various MRI solutions (5, 10, and 50 μM Mn) prepared in a sterile phosphate-buffered saline (PBS) solution, were treated into the cell culture media. Each treated volume of MRI solutions was ~2 μL. The treated cell culture media were then incubated for 48 h before the cell viability test. Each cell viability was normalized with respect to the control cell line with 0.0 M Mn concentration, respectively. This experiment was repeated three times.

Relaxivity and Map Image Measurements. A 1.5 T MRI instrument (GE Signa Advantage, GE Medical System) equipped with the Knee coil (EXTREM) was used to measure both the T_1 and T_2 relaxation times and the R_1 and R_2 map images. The measurement conditions have been described in detail previously (35). An inductively coupled plasma atomic emission spectrometer (ICPAES) (Thermo Jarrell Ash Co., IRIS/AP) was used to measure the Mn concentration of a MRI solution. Then, five MRI solutions diluted in distilled water (0.0625, 0.125, 0.25, 0.5, and 1.0 mM Mn) were prepared and then, used for both relaxation time and map image measurements. Both $1/T_1$ (= R_1) and $1/T_2$ (= R_2) inverse relaxation times (= relaxations) were plotted as a function of Mn concentration. The r_1 and r_2 relaxivities were then obtained from the slopes, respectively.

In vivo T_1 MR Image Measurement. The same 1.5 T MRI instrument equipped with a homemade small animal RF coil was used to take T_1 MR images. The coil was the receiver type with its inner diameter of 50 mm. The imaging parameters for T_1 3D fast SPGR (spoiled GRASS) images are as follows: repetition time (TR) = 9.2 ms; echo time (TE) = 4.2 ms; field of view (FOV) = 10 mm; matrix size = 256 × 192; slice thickness = 1.0 mm; number of acquisition (NEX) = 8. The in vivo animal study was performed in accordance with the rule of the animal research committee of Kyungpook National University. A six-week male ICR mouse with weight of 29−31 g was used. The mouse (n = 6) was anesthetized by 1.5% isoflurane in oxygen. Measurements were made before and after the injection of a MRI solution into a mouse tail vein. The injection dose was 0.07 mmol Mn/kg. After each measurement, the mouse was revived from anesthesia and placed in the cage with free access to both food and water. During measurement, the mouse was maintained at ~37 °C by using a warm water blanket.

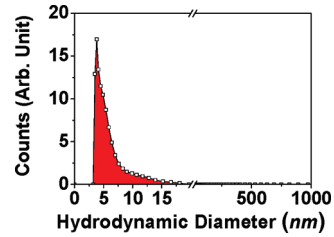

FIGURE 2. A DLS pattern of the MnO nanocolloid.

3. RESULTS AND DISCUSSION

Particle Diameter (d) of MnO Nanoparticle and the Hydrodynamic Diameter (a) of MnO Nanocolloid. HRTEM images show that the d of the MnO nanoparticle in the MnO nanocolloid is nearly monodisperse and ranges from 2 to 3 nm (Figure 1a−c). The measured lattice fringe (L) of 2.2 ± 0.1 Å is in a good agreement with the L_{200} (= 2.22 Å) of bulk cubic MnO (36, 37) (Figure 1c), showing that the synthesized nanoparticle is the cubic MnO. A DLS pattern shows that the average a of the MnO nanocolloid is 5.0 ± 0.1 nm, which is larger than the d of the MnO nanoparticle measured from HRTEM images due to both surface coating and hydration (Figure 2). The P of the MnO nanoparticle was estimated to be ~0.35 by using the average d (d_{avg}) of 2.5 nm estimated from HRTEM images, the average ionic diameter (t) of 0.22 nm of Mn(II) and O^{2-} ions (38), and a simple formula for P ($\approx 4(t/d_{avg})$).

Surface Coating. The MnO nanoparticle was coated with a biocompatible and hydrophilic D-glucuronic acid to protect it from its toxicity and for water-solubility. The surface coating was confirmed by recording a FTIR absorption spectrum of a powder sample (Figure 3a). The observed absorption frequencies characteristic of the D-glucuronic acid include the C−H stretch at ~2910 cm^{-1}, the C═O stretch at ~1600 cm^{-1}, and the C−O stretch at ~1080 cm^{-1}. A FTIR absorption spectrum of the free D-glucuronic acid was also recorded as a comparison (Figure 3b). Chemical bonding of carboxylic acids to various metal ions had been already verified by the red-shifted C═O stretch from the respective free carboxylic acids by various researchers (39−43). In the present case, a red-shift by ~110 cm^{-1} from the free D-glucuronic acid was observed. The amount of surface coating of the MnO nanoparticle with the D-glucuronic acid in the MnO nanocolloid was estimated to be 63% by recording a TGA curve of a powder sample (Figure 4a). The remaining 37% corresponds to the mass percentage of the MnO nanoparticle in the MnO nanocolloid. This shows that

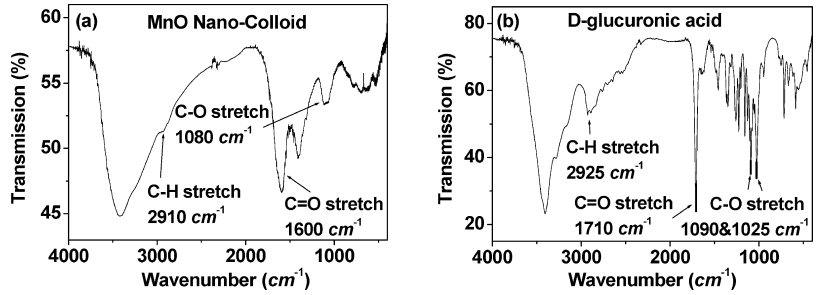

FIGURE 3. FTIR absorption spectra of powder samples of (a) the MnO nanocolloid and (b) the free D-glucuronic acid.

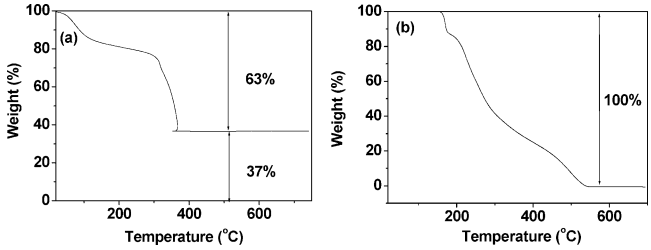

FIGURE 4. TGA curves of powder samples of (a) the MnO nanocolloid and (b) the free D-glucuronic acid.

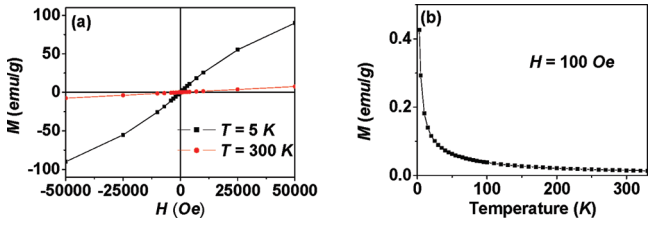

FIGURE 5. (a) $M-H$ and (b) $M-T$ curves of a powder sample of the MnO nanocolloid.

the MnO nanoparticle is sufficiently coated with the D-glucuronic acid. As a comparison, a TGA curve of free D-glucuronic acid is provided in Figure 4b. Above approximately 530 °C, all of the free D-glucuronic acid disappeared. Thus, the remaining mass after the TGA analysis of the powder sample is due to the MnO nanoparticle in the MnO nanocolloid.

Magnetic Properties. To characterize magnetic properties of the MnO nanoparticle in the MnO nanocolloid, both $M-H$ and ZFC $M-T$ curves were recorded as mentioned before (panels a and b in Figure 5, respectively). Here, magnetizations are net values of the MnO nanoparticle in the MnO nanocolloid as described in the experimental procedure. The $M-H$ curves show that both coercivity and remanence are zero. This lack of hysteresis as well as no magnetic transition down to $T = 3$ K in the ZFC $M-T$ curve shows that the MnO nanoparticle is mainly paramagnetic down to $T = 3$ K. From the $M-H$ curve at $T = 5$ K and at $H = 5$ T, magnetization of the MnO nanoparticle was estimated to be ~90 emu/g. Note that bulk MnO is antiferrimagnetic (44, 45). Also note that bulk spin structure is generally kept for nanosystems (46) except for surface metal ions, which used to be paramagnetic because of their unsaturated coordination. Thus, both paramagnetism and a large magnetic moment of the MnO nanoparticle are mainly attributed to its surface Mn(II) ions.

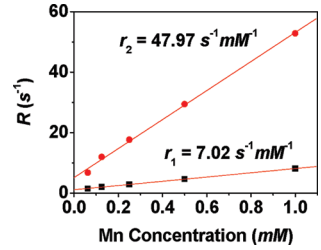

FIGURE 6. Plot of R_1 and R_2 relaxations of MRI solutions as a function of Mn concentration.

Table 1. Values of r_1 Relaxivities and r_2/r_1 Ratios of Various Chemicals

chemicals	ligand	d_{avg} (nm)	r_1 ($s^{-1}mM^{-1}$)	r_2/r_1	H (tesla)[a]	refs
Gd(III)-H_2O	DTPA[b]	NA[c]	4.1	1.1	1.5	7
Mn(II)-H_2O	EDTA[d]	NA	2.9		0.45	7
Gd_2O_3	D-glucuronic acid	1.0	9.9	1.1	1.5	16
Fe_3O_4	Dextran 40000	12	1.2	205.8	7.0	47
MnO	D-glucuronic acid	2.5	7.02	6.83	1.5	this work

[a] Applied magnetic field for relaxivity measurement. [b] Diethylenetriaminepentaacetic acid. [c] NA: not applicable. [d] Ethylenediaminetetraacetic acid.

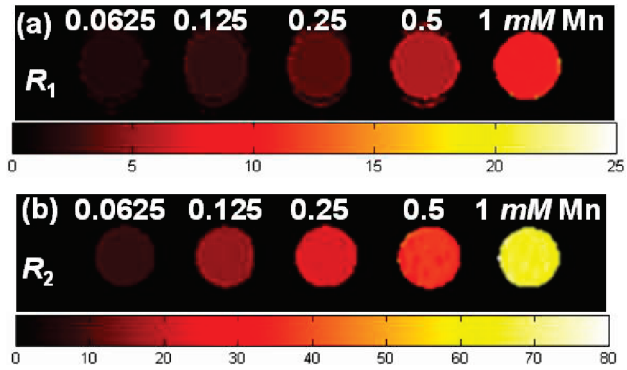

FIGURE 7. (a) R_1 and (b) R_2 map images of MRI solutions as a function of Mn concentration.

Relaxivities and Map Images. The r_1 and r_2 relaxivities of 7.02 and 47.97 s^{-1} mM^{-1} were obtained from the slopes in the plots of R_1 and R_2 relaxations as a function of Mn concentration, respectively (Figure 6), and are provided in Table 1. The R_1 and R_2 map images clearly showed dose-dependent contrast changes with increasing the dose (Figure 7a,b). These results indicate that the MnO nanocolloid should be a sensitive T_1 MRI contrast agent.

The r_1 relaxivities and the r_2/r_1 ratios of several representative chemicals are provided in Table 1 as a comparison.

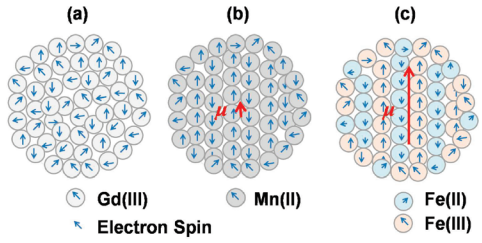

FIGURE 8. Spin structures of both surface and inside metal ions in (a) Gd_2O_3, (b) MnO, and (c) SPIO nanoparticles. Only the metal ions are shown (i.e., O^{2-} ions are omitted). Surface metal ions are paramagnetic for all of the nanoparticles. The Gd_2O_3 nanoparticle has no magnetic dipole (μ) because of its paramagnetic spin structure. The MnO nanoparticle has a tiny μ (indicated as a short arrow) because of incomplete spin cancellation of antiferromagnetic spins of its inside Mn(II) ions. The SPIO nanoparticle has a large μ (indicated as a long arrow) because of ferrimagnetic spin structure of its inside Fe(III)/Fe(II) ions.

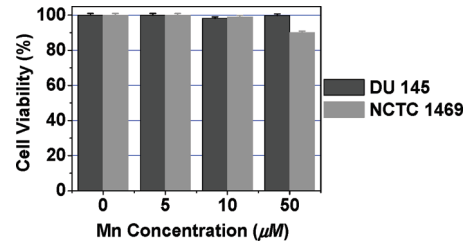

FIGURE 9. Cell viability of the MnO nanocolloid for Mn concentration from 0 to 50 μM.

First of all, the r_1 relaxivity of the MnO nanocolloid is higher than those of both molecular Mn(II)-EDTA and Gd(III)-DTPA chelates. Thia is primarily due to the densely populated Mn(II) ions in the MnO nanoparticle surface in the MnO nanocolloid. This corresponds to the common advantage of nanocolloids compared to molecular chelates. Here, the Gd(III)-DTPA is now clinically used (6).

The high r_1 relaxivity of the MnO nanocolloid can be understood from the three key-parameters for a T_1 MRI contrast agent which were discussed in the introduction section. The MnO nanocolloid very well satisfies them. That is, first, the Mn(II) ion has five unpaired *S*-state electrons, providing a high value of $S = 5/2$. Second, the MnO nanoparticle in the MnO nanocolloid was found to be mainly paramagnetic from its magnetic property analysis. Third, the MnO nanoparticle with the d_{avg} of 2.5 *nm* has a decent value of P (≈ 0.35) as mentioned before.

The MnO nanocolloid has different r_1 and r_2 relaxivities from those of the Gd_2O_3 and the SPIO nanocolloids. This difference can be also accounted for through the three key-parameters. Let us consider the r_1 relaxivity. First, the Gd(III), the Mn(II), the Fe(III), and the Fe(II) ions have $S = 7/2$, 5/2, 5/2, and 2, respectively (31). Here, the first three ions consist of purely *S*-state electrons, whereas the last Fe(II) ion consists of *L*-state electrons with $L = 2$. Thus, only the Fe(III) ions in the SPIO nanocolloid will mainly contribute to the r_1 relaxivity because *L*-state electrons are not efficient in inducing the longitudinal water proton relaxation as mentioned before (6, 30). Note that the r_1 relaxivity is proportional to $S(S + 1)$ as mentioned before (7). Thus, the first parameter is satisfied in the order of Gd_2O_3 > MnO > SPIO nanocolloids. Second, the Gd_2O_3, MnO, and SPIO nanoparticles are paramagnetic, nearly paramagnetic, and superparamagnetic, respectively. Here, the superparamagnetic SPIO nanoparticle has a ferrimagnetic spin structure, thus having a large *M*, which is not good for the longitudinal water proton relaxation. Thus, the second parameter is satisfied in the order of Gd_2O_3 > MnO $\gg$ SPIO nanocolloids. Third, the third parameter is also satisfied in the same order of the Gd_2O_3 > MnO $\gg$ SPIO nanocolloids, referring to the d_{avg} provided in Table 1. Taking all of these into account, the r_1 relaxivity will be in the order of r_1 (Gd_2O_3 nanocolloid) > r_1 (MnO nanocolloid) $\gg$ r_1 (SPIO nanocolloid), which is consistent with the observed order in Table 1. Let us consider the r_2 relaxivity. It is proportional to M^2 (32). Thus, a nanoparticle should have a large *M*. The three key parameters for this include a large *S* because *M* is the vector sum of all the $\sqrt{S(S + 1)}$ of metal ions, a ferromagnetic or a ferrimagnetic spin structure, and a small *P* of a nanoparticle as mentioned before. The combined effect of the first and second parameters on the *M* are shown in Figure 8a–c. That is, the Gd_2O_3 nanoparticle has $M = 0$ (or no magnetic dipole (μ)) because of its paramagnetic spin structure (48). The MnO nanoparticle may have a tiny *M* (or a tiny μ) because of incomplete spin cancellation of antiferromagnetic spins of its inside Mn(II) ions (44–46). The SPIO nanoparticle will have a large *M* (or a large μ) because of ferrimagnetic spin structure of its inside Fe(III)/Fe(II) ions (26–28). Because the *M* is proportional to the *d*, the r_2 relaxivity will be in the order of r_2 (SPIO nanocolloid) $\gg$ r_2 (MnO nanocolloid) > r_2 (Gd_2O_3 nanocolloid), which is consistent with the observed order in Table 1.

Although the MnO nanocolloid seems to be a less sensitive T_1 MRI contrast agent than the Gd_2O_3 nanocolloid because of its lower r_1 relaxivity and higher r_2/r_1 ratio than those of the Gd_2O_3 nanocolloid, it is still the potential candidate for a sensitive T_1 MRI contrast agent because it has a higher r_1 relaxivity than the clinically used Gd(III)-chelates. Furthermore, the Mn(II) ion is much less toxic than the Gd(III) ion. Note that $MnCl_2$ is used as a T_1 MRI contrast agent for animal (33, 49–51).

In vitro Cytotoxicity. For the MnO nanocolloid to be safely applied in vivo, it should be nontoxic. We performed an in vitro cytotoxicity test of the MnO nanocolloid by using the human prostate cancer (DU145) and the mouse normal hepatocyte (NCTC1469) cell lines as mentioned before. As shown in Figure 9, the MnO nanocolloid is not toxic for the tested concentration range up to 50 μM Mn.

In vivo T_1 MR Images of a Mouse. We finally carried out an in vivo test of a MRI solution by injecting it into a mouse tail vein and then, taking 1.5 T in vivo T_1 MR images. A series of 1.5 T in vivo T_1 MR images are provided in Figure 10. These T_1 MR images clearly show high contrast enhancements at various organs after injection. It is not accumulated into a liver due to its small size, though conventional large nanocolloids are mostly accumulated into liver and spleen (52–56). The contrast at various organs including kidneys and liver (indicated in Figure 10) initially became enhanced, but then decreased as time passed. That is, all body showed a significant contrast enhancement at 5 min after injection of the MRI solution. The contrast enhancement of both the

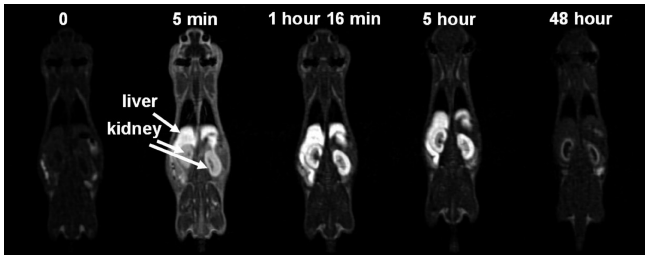

FIGURE 10. A series of 1.5 T in vivo T_1 MR images of a mouse with time after injection of a MRI solution into a mouse tail vein.

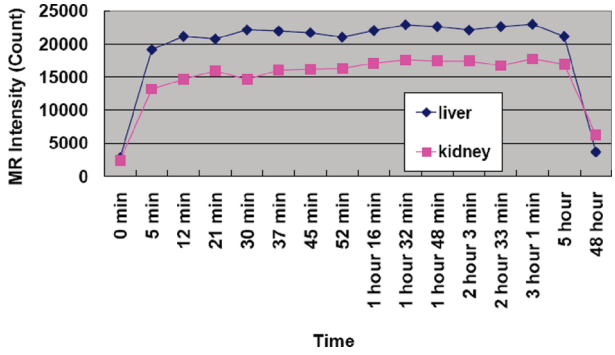

FIGURE 11. MR signal intensity variations with time in both liver and kidneys after injection of a MRI solution into a mouse tail vein.

kidneys and liver was maintained up to 5 h. Finally, the T_1 MR images taken at 48 h after injection show that the contrast enhancement in the liver almost disappeared and the contrast enhancement in the kidneys also largely disappeared. This is due to the excretion of the MnO nanocolloid through the kidneys, which is prerequisite for clinical application. The MR signal intensity variations with time in both kidneys and liver are also plotted in Figure 11 to clearly show this. This in vivo result implies that the MnO nanocolloid may function as a sensitive T_1 MRI contrast agent.

4. CONCLUSION

We presented a facile one-pot synthesis of a water-soluble MnO nanocolloid. The MnO nanoparticle in the MnO nanocolloid was coated with a biocompatible and hydrophilic D-glucuronic acid, and its d was nearly monodisperse and ranged from 2 to 3 nm. The average a of the MnO nanocolloid was estimated to be 5 nm. The MnO nanoparticle was nearly paramagnetic down to 3 K and showed a high magnetic moment of ~90 emu/g at $T = 5$ K and $H = 5$ T, which mainly arises from surface Mn(II) ions with $S = 5/2$ as well as a decent P (≈ 0.35) of the MnO nanoparticle. For these reasons, a high r_1 relaxivity of 7.02 s^{-1} mM^{-1} was observed. This value is higher than those of the clinically used metal ion chelate MRI contrast agents. The observed r_2 relaxivity of 47.97 s^{-1} mM^{-1} is likely due to a tiny M of the MnO nanoparticle arising from incomplete spin cancellation of antiferromagnetic spins of its inside Mn(II) ions. In vivo testing of an MRI solution showed high contrast T_1 MR images, proving that the MnO nanocolloid functions as a sensitive T_1 MRI contrast agent. The three key parameters that control the r_1 and r_2 relaxivities of nanocolloids were suggested. These include the S value of a metal ion, the spin structure, and the P of a nanoparticle. The r_1 and r_2 relaxivities of the MnO nanocolloid as well as those of the Gd_2O_3 and the SPIO nanocolloids were qualitatively well-accounted for by using these parameters. This indicates that these parameters will be extremely valuable in designing a nanocolloidal MRI contrast agent.

Acknowledgment. This work was supported by Grant RTI04-01-01 from the Regional Technology Innovation Program of the Ministry of Commerce, Industry, and Energy funded by the Korean Government, the Basic Science Research Program through the National Research Foundation (NRF) funded by the Ministry of Education, Science and Technology (2010-0002436), and the Ministry for Health, Welfare & Family Affairs through the Korea Healthcare technology R&D Project (Grant A090193). We thank the Korea Basic Science Institute for allowing us to use their HRTEM.

REFERENCES AND NOTES

(1) Kouassi, G. K.; Irudayaraj, J. *J. Nanobiotechnol.* **2006**, *4*, 8.
(2) Pankhurst, Q. A.; Connolly, J.; Jones, S. K.; Dobson, J. *J. Phys. D.: Appl. Phys.* **2003**, *36*, R167–R181.
(3) Doyle, P. S.; Bibette, J.; Bancaud, A.; Viovy, J.-L. *Science* **2002**, *295*, 2237.
(4) Salata, O. V. *J. Nanobiotechnol.* **2004**, *2*, 3.
(5) Pankhurst, Q. A.; Thanh, N. K. T.; Jones, S. K.; Dobson, J. *J. Phys. D.:Appl. Phys.* **2009**, *42*, 224001–224015.
(6) Caravan, P.; Ellison, J. J.; McMurry, T. J.; Lauffer, R. B. *Chem. Rev.* **1999**, *99*, 2293–2352.
(7) Lauffer, R. B. *Chem. Rev.* **1987**, *87*, 901–927.
(8) Resovist from Schering AG, Germany.
(9) Lee, J.-H.; Huh, Y.-M.; Jun, Y.-W.; Seo, J.-W.; Jang, J.-T.; Song, H.-T.; Kim, S.; Cho, E.-J.; Yoon, H.-G.; Suh, J.-S.; Cheon, J. *Nat. Med.* **2007**, *13*, 95–99.
(10) Na, H. B.; Lee, J. H.; An, K.; Park, Y. I.; Park, M.; Lee, I. S.; Nam, D.-H.; Kim, S. T.; Kim, S.-H.; Kim, S.-W.; Lim, K.-H.; Kim, K.-S.; Kim, S.-O.; Hyeon, T. *Angew. Chem., Int. Ed* **2007**, *46*, 5397–5401.
(11) Engström, M.; Klasson, A.; Pedersen, H.; Vahlberg, C.; Käll, P.-O.; Uvdal, K. *Magn. Reson. Mater. Phys.* **2006**, *19*, 180–186.
(12) Fortin, M.-A.; Petoral, R. M.; Söderlind, F.; Klasson, A.; Engström, M.; Veres, T.; Käll, P.-O.; Uvdal, K. *Nanotechnology* **2007**, *18*, 395501.
(13) Petoral, R. M.; Söderlind, F.; Klasson, A.; Suska, A.; Fortin, M. A.; Abrikossova, N.; Selegård, L.; Käll, P.-O.; Engström, M.; Uvdal, K. *J. Phys. Chem. C* **2009**, *113*, 6913–6920.
(14) Bridot, J.-L.; Faure, A.-C.; Laurent, S.; Rivière, C.; Billotey, C.; Hiba, B.; Janier, M.; Josserand, V.; Coll, J.-L.; Elst, L. V.; Muller, R.; Roux, S.; Perriat, P.; Tillement, O. *J. Am. Chem. Soc.* **2007**, *129*, 5076–5084.
(15) Miyawaki, J.; Yudasaka, M.; Imai, H.; Yorimitsu, H.; Isobe, H.; Nakamura, E.; Lijima, S. *J. Phys. Chem. B* **2006**, *110*, 5179–5181.
(16) Park, J. Y.; Baek, M. J.; Choi, E. S.; Woo, S.; Kim, J. H.; Kim, T. J.; Jung, J. C.; Chae, K. S.; Chang, Y.; Lee, G. H. *ACS Nano* **2009**, *3*, 3663–3669.
(17) Li, I.-F.; Su, C.-H.; Sheu, H.-S.; Chiu, H.-C.; Lo, Y.-W.; Lin, W.-T.; Chen, J.-H.; Yeh, C.-S. *Adv. Funct. Mater* **2008**, *18*, 766–776.
(18) Hu, K.-W.; Jhang, F.-Y.; Su, C.-H.; Yeh, C.-S. *J. Mater. Chem* **2009**, *19*, 2147–2153.
(19) Ahrén, M.; Selegård, L.; Klasson, A.; Söderlind, F.; Abrikossova, N.; Skoglund, C.; Bengtsson, T.; Engström, M.; Käll, P.-O.; Uvdal, K. *Langmuir* **2010**, *26*, 5753–5762.
(20) Rieter, W. J.; Taylor, K. M. L.; An, H.; Lin, W.; Lin, W. *J. Am. Chem. Soc.* **2006**, *128*, 9024–9025.
(21) Li, I.-F.; Yeh, C.-S. *J. Mater. Chem* **2010**, *20*, 2079–2081.
(22) Hifumi, H.; Yamaoka, S.; Tanimoto, A.; Citterio, D.; Suzuki, K. *J. Am. Chem. Soc.* **2006**, *128*, 15090–15091.
(23) Evanics, F.; Diamente, P. R.; van Veggel, F. C. J. M.; Stanisz, G. J.; Prosser, R. S. *Chem. Mater.* **2006**, *18*, 2499–2505.
(24) Gossuin, Y.; Hocq, A.; Vuong, Q. L.; Disch, S.; Hermann, R. P.'; Gillis, P. *Nanotechnology* **2008**, *19*, 475102.

(25) Norek, M.; Kampert, E.; Zeitler, U.; Peters, J. A. *J. Am. Chem. Soc.* **2008**, *130*, 5335–5340.
(26) Li, Q.; Sorensen, C. M.; Klabunde, K. J.; Hadjipanayis, G. C. *Aerosol Sci. Technol.* **1993**, *19*, 453–467.
(27) Zhang, D.; Klabunde, K. J.; Sorensen, C. M.; Hadjipanayis, G. C. *Phys. Rev. B* **1998**, *58*, 14167–14170.
(28) Gangopadhyay, S.; Hadjipanayis, G. C.; Dale, B.; Sorensen, C. M.; Klabunde, K. J.; Papaefthymiou, V.; Kostikas, A. *Phys. Rev. B* **1992**, *45*, 9778–9786.
(29) The r_2/r_1 ratio is always greater than 1.0 because the T_2/T_1 relaxation time is always less than 1.0. See Hashemi, R. H.; Bradley, W. G.; Lisanti, C. J. *MRI: The Basics*, 2nd ed.; Lippincott Williams & Wilkins; Philadelphia, PA, 2004; pp 42−43.
(30) Banci, L.; Bertini, I.; Luchinat, C. *Nuclear and Electron Relaxation*; VCH: Weinheim, Germany, 1991.
(31) Cotton, F. A.; Wilkinson, G. *Advanced Inorganic Chemistry*; John Wiley & Sons: New York, 1980.
(32) Roch, A.; Gossuin, Y.; Muller, R. N.; Gillis, P. *J. Magn. Magn. Mater.* **2005**, *293*, 532–539.
(33) Strijkers, G. J.; Mulder, W. J. M.; van Tilborg, G. A. F.; Nicolay, K. *Anti-Cancer Agents Med. Chem.* **2007**, *7*, 291–305.
(34) Seo, W. S.; Jo, H. H.; Lee, K.; Kim, B.; Oh, S. J.; Park, J. T. *Angew. Chem., Int. Ed.* **2004**, *43*, 1115–1117.
(35) Park, J. Y.; Daksha, P.; Lee, G. H.; Woo, S.; Chang, Y. *Nanotechnology* **2008**, *19*, 365603.
(36) Moore, T. E.; Ellis, M.; Selwood, P. W. *J. Am. Chem. Soc.* **1950**, *72*, 856–866.
(37) JCPDS-International Center for Diffraction Data, Card no. 01−1206, PCPDFWIN, vol. 1.30, 1997.
(38) Dean, J. A. *Lange's Handbook of Chemistry*; McGraw-Hill: New York, 1992.
(39) Söderlind, F.; Pedersen, H.; Petoral, R. M.; Käll, P.-O.; Uvdal, K. *J. Colloid Interface Sci.* **2005**, *288*, 140–148.
(40) Mendive, C. B.; Bredow, T.; Blesa, M. A.; Bahnemann, D. W. *Phys. Chem. Chem. Phys.* **2006**, *8*, 3232–3247.
(41) Hug, S. J.; Bahnemann, D. *J. Electron Spectrosc.* **2006**, *150*, 208–219.
(42) Duckworth, O. W.; Martin, S. C. *Geochim. Cosmochim. Acta* **2001**, *65*, 4289–4301.
(43) Roddick-Lanzilotta, A. D.; McQuillan, A. J. *J. Colloid Interface Sci.* **1999**, *217*, 194–202.
(44) Neubeck, W.; Ranno, L.; Hunt, M. B.; Vettier, C.; Givord, D. *Appl. Surf. Sci.* **1999**, *138*, 195–198.
(45) Towler, M. D.; Allan, N. L.; Harrison, N. M.; Saunders, V. R.; Mackrodt, W. C.; Aprà, E. *Phys. Rev. B* **1994**, *50*, 5041–5054.
(46) Kodama, R. H.; Makhlouf, S. A.; Berkowitz, A. E. *Phys. Rev. Lett.* **1997**, *79*, 1393–1396.
(47) Chapon, C.; Franconi, F.; Lemaire, L.; Marescaux, L.; Legras, P.; Saint-André, J. P.; Denizot, B.; Le Jeune, J.-J. *Invest. Radiol* **2003**, *38*, 141–146.
(48) Moon, R. M.; Koehler, W. C. *Phys. Rev. B* **1975**, *11*, 1609–1622.
(49) Silva, A. C.; Lee, J. H.; Aoki, I.; Koretsky, A. P. *NMR Biomed.* **2004**, *17*, 532–543.
(50) Crossgrove, J.; Zheng, W. *NMR Biomed.* **2004**, *17*, 544–553.
(51) Goldman, M. R.; Brady, T. J.; Pykett, I. L.; Burt, C. T.; Buonanno, F. S.; Kistler, J. P.; Newhouse, J. H.; Hinshaw, W. S.; Pohost, G. M. *Circulation* **1982**, *66*, 1012–1016.
(52) Magin, R. L.; Bacic, G.; Niesman, M. R.; Alameda, J. C.; Wright, S. M.; Swartz, H. M. *Magn. Reson. Med.* **1991**, *20*, 1–16.
(53) Widder, D. J.; Greif, W. L.; Widder, K. J.; Edelman, R. R.; Brady, T. J. *AJR* **1987**, *148*, 399–404.
(54) Saini, S.; Stark, D. D.; Hahn, P. F.; Bousquet, J. C.; Introcasso, J.; Wittenberg, J.; Brady, T.; Ferrucci, J. T. *Radiology* **1987**, *162*, 217–222.
(55) Hemmingsson, A.; Carlsten, J.; Ericsson, A.; Klaveness, J.; Sperber, G. O.; Thuomas, K. A. *Acta Radiol.* **1987**, *28*, 703–705.
(56) Weissleder, R.; Hahn, P. F.; Stark, D. D.; Elizondo, G.; Saini, S.; Todd, L. E.; Wittenberg, J.; Ferrucci, J. T. *Radiology* **1988**, *169*, 399–403.

AM100641Z